Cobalt phosphide nanowires as efficient co-catalyst for photocatalytic hydrogen evolution over $Zn_{0.5}Cd_{0.5}S$

Pengfei Wang[a], Sihui Zhan[a,*], Haitao Wang[a], Yuguo Xia[b], Qianlei Hou[a], Qixing Zhou[a,*], Yi Li[c], Ramasamy Rajesh Kumar[a]

[a] MOE Key Laboratory of Pollution Processes and Environmental Criteria/Tianjin Key Laboratory of Environmental Remediation and Pollution Control, College of Environmental Science and Engineering, Nankai University, Tianjin 300350, PR China
[b] School of Chemistry & Chemical Engineering, National Engineering Research Center for Colloidal Materials, Shandong University, Jinan 250100, PR China
[c] Department of Chemistry, Tianjin University, Tianjin 300072, PR China

ARTICLE INFO

ABSTRACT

Previous studies have shown that co-catalysts play a pivotal role for improving both the activity and reliability of semiconductors in photocatalytic hydrogen production, however, designing highly efficient and cost-effective co-catalysts to replace expensive and rare metals is still a big challenge. In this work, DFT (density functional theory) is utilized to guide the application of CoP NWs (nanowires) as an earth-abundant co-catalyst for photocatalytic hydrogen production. Metallic 1D CoP NWs is rationally integrated with $Zn_{0.5}Cd_{0.5}S$ solid solution semiconductor for the first time, to induce a remarkably improved photocatalytic hydrogen production activity of 12,175.8 μmol h^{-1} g^{-1}, which is 22 times higher than that of the pristine $Zn_{0.5}Cd_{0.5}S$. This outstanding activity benefits from the collaborative advantages of excellent metallic conductivity and the rigid 1D nanostructure of CoP NWs. Moreover, the mechanism investigations demonstrate that this excellent activity arises from the strong electronic coupling, favourable band structure, highly efficient charge separation and migration based on the powerful characterizations, such as time-resolved PL decay spectra and photoelectrochemical methodology. This work brings new opportunities to employ 1D co-catalysts on photocatalysts for improving the catalytic activities in hydrogen production from water.

1. Introduction

Due to the zero carbon content, hydrogen has been considered to be a promising energy supply for solving global energy problems [1]. Especially, photocatalytic water splitting by using semiconductors has demonstrated great potential as a promising strategy for producing clean and carbon-neutral hydrogen fuel since the photoelectrochemical water splitting was discovered in 1972 by Honda and Fujishima [2]. To date, although kinds of impressive semiconductors have been developed [3], it still require great efforts to explore highly efficient, cost-effective and stable photocatalysts driven by natural light. Recent studies have shown that co-catalysts play a significant role in improving both the activity and stability of semiconductor photocatalysts. Currently, noble-metal-based co-catalysts including Ru [4], Rh [5], Pd [6], Pt [7–9], Au [10] and Ag [11] have been extensively investigated for photocatalytic hydrogen production. Unfortunately, the above noble-metal based co-catalysts are too rare and expensive, and the commercialization of current photocatalysts has been seriously restricted.

Therefore, seeking noble-metal free and earth-abundant co-catalysts with high efficiency and low cost is of great significance for large-scale energy production.

To date, various earth-abundant co-catalysts have been employed to combine with photocatalysts, including transition metals, transition metal compounds (e.g. transition metal oxides, hydroxides, sulfides, carbides and phosphides) and nanocarbon-based co-catalysts [2,12–18]. However, most of the co-catalysts are 0D particles. Although the employment of 0D co-catalysts can actually enhance the photocatalytic performance, these particles are difficult to homogeneously disperse on the surface of photocatalysts, and the 0D nanoparticles have a tendency to agglomerate and some large clusters with irregular agglomerate are universal. In this context, targeted engineering of co-catalysts with different structure and morphology has obtained great attention, because the microscopic structural and morphology factors have synergistic impacts on the photocatalysts. Therefore, considering the basic mantra of "structure-dictates-function" in chemistry, it is urgent to design efficient co-catalysts with desirable architectural

structure/morphology toward photocatalytic hydrogen production.

In view of high surface-to volume ratio and excellent electron transport property, one dimensional (1D) nanostructured materials are believed to play an important role in the next-generation building blocks for electronic devices, solar cells, photocatalysis and lithium-ion batteries. CoP NWs (nanowires), an important metal phosphides with good electrical conductivity, has shown great potential as electrocatalyst in hydrogen evolution reaction [18,19]. Notably, the distinguished characteristics of CoP NWs render them highly promising for photocatalytic hydrogen production: (i) the smaller overpotential of CoP NWs is beneficial to hydrogen production reactions on the surface of photocatalysts; (ii) the excellent metallic conductivity of CoP NWs assures efficient charge-carrier transfer; (iii) the acid-stability of CoP NWs is beneficial to hydrogen production in acid aqueous solution. Given the outstanding properties of CoP NWs, it can be predicted that CoP NWs will be a promising co-catalyst to be applied in photocatalysis. However, to the best of our knowledge, there is no exploring CoP NWs as a co-catalyst for photocatalytic hydrogen production.

Herein, we report a highly stable and inexpensive photocatalytic system with CoP NWs as the co-catalyst, $Zn_{0.5}Cd_{0.5}S$ solid solution as the photocatalyst and ascorbic acid as the electron donor. And an excellent photocatalytic hydrogen production activity was obtained from CoP NWs system, whose hydrogen production performance was much higher than CoP NPs system, which was studied by both theoretical and experimental studies.

2. Experimental section

2.1. Preparation of $Co(CO_3)_{0.35}Cl_{0.20}(OH)_{1.10}$, Co_3O_4 and CoP nanowires

All chemicals were of analytical grade and were directly used as received without further purification. $Co(CO_3)_{0.35}Cl_{0.20}(OH)_{1.10}$ nanowires were prepared according to reported method with minor modifications [19]. Typically, 5 mmol $CoCl_2·6H_2O$ and 5 mmol urea were dissolved in 40 mL distilled water under stirring. The solution was transferred to a 100 mL Teflon-lined autoclave and the autoclave was sealed and maintained at 100 °C for 12 h in an electric oven. After the autoclave cooled down naturally at room temperature, the resulting pink precipitate was collected and washed with water and ethanol several times by centrifugation and dried at 60 °C for 8 h. Then $Co(CO_3)_{0.35}Cl_{0.20}(OH)_{1.10}$ nanowires were calcinated at 400 °C for 2 h in air to obtain Co_3O_4 nanowires. To prepare CoP nanowires, Co_3O_4 nanowires and NaH_2PO_2 were put at two separate positions in a porcelain boat in the presence of NaH_2PO_2 at the upstream side of the furnace. The molar ratio for Co to P was 1:5. After flushed with N_2, the center of the furnace was heated to 300 °C for 2 h under a static N_2 atmosphere. The resulting CoP nanowires were collected after cooling to ambient temperature under N_2 and were labeled as CoP NWs.

2.2. Preparation of CoP nanoparticles

CoP nanoparticles were prepared according to reported method with minor modifications [20]. Briefly, 5 mmol $CoCl_2·6H_2O$ and 20 mmol NaH_2PO_2 were mixed together in an agate mortar and grunded to a fine mixture. Then the mixture was heated to 400 °C for 2 h under a static N_2 atmosphere. After cooling to room temperature, the sample was washed with water and ethanol several times by centrifugation and dried at 60 °C for 8 h. The resulting CoP nanoparticles were labeled as CoP NPs.

2.3. Preparation of $Zn_{0.5}Cd_{0.5}S$ solid solution

$Zn_{0.5}Cd_{0.5}S$ solid solution was prepared according to reported method with minor modifications [12]. In a typical procedure, 5 mmol $Zn(Ac)_2·2H_2O$, 5 mmol $Cd(Ac)_2·2H_2O$ and 12.5 mmol thioacetamide were dissolved in 40 mL distilled water under stirring. Then 10 mL 4 M

NaOH aqueous solution was added into the above solution under strong stirring until a homogeneous solution was formed. The solution was transferred to a 100 mL Teflon-lined autoclave and the autoclave was sealed and maintained at 180 °C for 24 h in an electric oven. After the autoclave cooled down naturally at room temperature, the resulting yellow product was collected and washed with water and ethanol several times by centrifugation and dried at 60 °C for 8 h. The resulting $Zn_{0.5}Cd_{0.5}S$ solid solution was labeled as ZCS.

2.4. Preparation of $Zn_{0.5}Cd_{0.5}S/CoP$ NWs and NPs composites

Preparation of $Zn_{0.5}Cd_{0.5}S/CoP$ NWs and NPs composites were prepared according to reported method with minor modifications [21]. Briefly, 0.3 g $Zn_{0.5}Cd_{0.5}S$ powder was dispersed into 50 mL distilled water in an ultrasound bath for 60 min. Then a certain amount of CoP NWs was added into the suspension under constantly stirring. After 2 h continuous stirring, the resulting ZCS/x% CoP NWs (x represents CoP NWs amount, x = 2, 4, 6, 8, 10, 12) were collected by centrifugation and dried at 60 °C for 12 h. And ZCS/x% CoP NPs was obtained by the same method.

2.5. Theoretical calculation

First-principles calculations were performed by using density functional theory (DFT) with the generalized gradient approximation (GGA) for the exchange-correlation function as formulated by Perdew, Burke and Ernzerof (PBE). The valence electron-ion interaction was modeled by the projector augmented wave (PAW) potential as implemented in the Vienna ab initio simulation pakage (VASP). For all the calculations, both the lattice constant and the positions of all atoms are relaxed until the force is less than 0.22 eV/Å. The criterion for the total energy is set as 1×10^{-5} eV.

2.6. Characterization

Scanning electron microscopy (SEM) was performed using a Hitachi SU8010 at an accelerating voltage of 3 kV (Japan) to observe the morphology of the prepared samples. High-resolution transmission electron microscopy (TEM and HRTEM) analyses were conducted using a JEOL JEM-2100F at an accelerating voltage of 200 kV (Japan) to analyze the microstructure of the samples. XRD patterns were obtained using a Rigaku D/Max 2200PC X-ray diffractometer (XRD) with Cu Kα radiation (λ = 0.15418 nm) to obtain the crystalline structure of the samples. The Brunauer-Emmett-Teller (BET) specific surface areas of the samples were measured using a Micromeritics ASAP 2460 system at liquid nitrogen temperature. The pore size distributions were estimated form desorption isotherms by the Barret-Joyner-Halenda (BJH) method, assuming a cylindrical pore model. XPS measurements were performed in a Thermal ESCALAB 250 electron spectrometer using Al Kα radiation X-ray source (hν = 1486.6 eV) to determine the valence states of all elements. UV–vis diffused reflectance spectra of the samples were obtained using a Shimadzu Corporation UV–vis spectrophotometer to record the absorption spectra of the samples. Fourier transform infrared spectra (FTIR) were recorded for the samples using a Thermo Nicolet iS5 FTIR spectrometer equipped with a liquid-nitrogen-cooled MCT detector. Steady-state photoluminescence (PL) spectra were measured using an Edinburgh Instruments FLS920P equipped with a Xe lamp-920 at room temperature under the excitation of 360 nm. Time-resolved PL decay curves were recorded on a FLS920 fluorescence lifetime spectrophotometer under the excitation of 360 nm and probed at 545 nm.

2.7. Photocatalytic hydrogen production

The photocatalytic hydrogen test was carried out in a closed system with a 150 mL quartz flask. A full spectrum solar simulator (CEL-S500)

with AM 1.5G filter, which was about 1 Sun power, was used to provide incident light and the area of the surface irradiated in the cylinder reactor was about 17.8 cm^2. In a typical photocatalytic experiment, 100 mg of photocatalyst powder was suspended with a constant stirring in 100 mL aqueous solution containing 20 vol. % 0.75 M ascorbic acid as sacrificial electron donor. Then the reaction system was thoroughly degassed by evacuation. Next, the mixture was illuminated under continuous magnetic stirring and a water-cooling filter was used to keep the reaction temperature at ca. 10 °C. The generated gas spread into the quantitative loop (1 mL) of a six-way valve, and the gas volume was analyzed by gas chromatography equipped with a thermal conductive detector every 60 min to determine the hydrogen generation rate.

The apparent quantum efficiency (QE) at a wavelength of 365 nm, 420 nm, 475 nm and 520 nm was measured under the identical reaction condition by placing various band-pass filters in front of the light source. The CEL-NP2000 spectroradiometer was used to measure the intensity of the incident light. The apparent QE was calculated according to the following equation [22]:

$$QE[\%] = \frac{number\ of\ reacted\ electrons}{number\ of\ incident\ photons} \times 100$$

$$= \frac{number\ of\ evolved\ H_2\ molecules \times 2}{number\ of\ incident\ photons} \times 100$$

2.8. Photoelectrochemical measurements

The working photoanodes were fabricated as follows: 4 mg sample, 1 mL ethanol and 20 μl nafion were mixed by sonication for 30 min to make a slurry. The slurry was then dropped onto an indium-tin oxide (ITO) glass. After the ethanol evaporated thoroughly at ambient temperature, the photoanodes were dried at 60 °C for 8 h. The active areas of the photoanodes are ca. 2.75 cm^2. Photoelectrochemical (PEC) performances of the prepared photoanodes were recorded on an electrochemical work station (CHI660E Instruments) with a standard three-electrode system (an Ag/AgCl electrode reference electrode and a Pt foil counter electrode). 0.5 M NaSO$_4$ solution was used as the electrolyte. The measured potential vs. Ag/AgCl was converted to reversible hydrogen electrode (RHE) scale using the Nernst equation: $E_{RHE} = E_{Ag/AgCl} + 0.197 + 0.059\ pH$. A 300 W Xe lamp was used as a light source. Typically, polarization curves were recorded at a scan rate of 5 mV s^{-1} and the chopped illumination was used to examine transient photocurrents. Transient photocurrent measurements with chopped illumination were also conducted to examine the steady-state photocurrent densities of the photoanodes. Electrochemical impedance spectra (EIS) were carried out in the frequency range of $0.05 - 10^5$ Hz.

3. Results and discussion

### 3.1. Theoretical and experimental exploration of CoP NWs as a co-catalyst

CoP NWs was obtained by a low-temperature phosphidation of Co$_3$O$_4$ NWs, which was acquired by calcining a hydrothermally synthesized Co(CO$_3$)$_{0.35}$Cl$_{0.20}$(OH)$_{1.10}$, as illustrated in Scheme 1. Firstly, CoCl$_2$ and the morphology inducer, CO(NH$_2$)$_2$, were dissolved in water and tightly coupled. After hydrothermal reaction at 100 °C, the purple cobalt precursor, Co(CO$_3$)$_{0.35}$Cl$_{0.20}$(OH)$_{1.10}$, formed. Then, the cobalt precursor was calcined at 400 °C, and during this process, Co(CO$_3$)$_{0.35}$Cl$_{0.20}$(OH)$_{1.10}$ was subjected to thermal decomposition and oxidization, thus yielding crystalline Co$_3$O$_4$. Following phosphidation of Co$_3$O$_4$ at 300 °C under nitrogen atmosphere, black CoP NWs was obtained by the successful chemical conversion of Co$_3$O$_4$ NWs.

The crystal structures during the preparation of CoP NWs were characterized by X-ray diffraction (XRD) experiments (Fig. 1a). The hydrothermal product shows diffraction peaks indexed to Co

(CO$_3$)$_{0.35}$Cl$_{0.20}$(OH)$_{1.10}$ [19]. And the calcined sample exhibits peaks indexed to Co$_3$O$_4$(JCPDS 09-0418). Following phosphidation, only peaks corresponding to orthorhombic CoP are observed (JCPS-65-2593). And the peaks at 32°, 35°, 36°, 46°, 48°, 52°, 56° and 57° are indexed to the (011), (200), (111), (112), (211), (103), (020) and (301) planes of CoP, respectively. These transformations of crystal structures confirm the successful chemical conversion of Co$_3$O$_4$ to CoP NWs. There is no IR signal of Co(CO$_3$)$_{0.35}$Cl$_{0.20}$(OH)$_{1.10}$ remaining in the spectrum of CoP NWs, indicating the complete decomposition of Co(CO$_3$)$_{0.35}$Cl$_{0.20}$(OH)$_{1.10}$ (Fig. S2). And the CoP NPs shows the similar XRD peaks to CoP NWs (Fig. S1a), indicating the successful preparation of CoP NPs.

The morphology of the as-prepared samples was thoroughly investigated by SEM and TEM techniques. As revealed by the image of low-magnification SEM (Fig. 1b), Co(CO$_3$)$_{0.35}$Cl$_{0.20}$(OH)$_{1.10}$ NWs consists of 1D nanostructures with a length of several micrometers. The high-magnification SEM image (inset) reveals the nanowires with a diameter in the range of 200–300 nm are formed. And for Co$_3$O$_4$ NWs (Fig. 1c), the surface becomes rough and the length decreases. After phosphidation, the high-magnification SEM image and the TEM image (Fig. 1d inset and Fig. 1e) reveal that the CoP NWs has diameters about 100 nm and they still preserve 1D nanostructures. The high-resolution TEM (HRTEM) image of CoP NWs (Fig. 1f) shows a lattice spacing of ca. 2.83 Å, which belongs to the (011) diffraction plane of CoP [23]. And Fig. 1g shows the elemental mapping images of P and Co for CoP NWs, indicating that both elements, phosphorus and cobalt, are uniformly distributed in the whole nanowire.

We next carried out a series of methods to compare the potential of CoP NWs and CoP NPs for co-catalysts in photocatalytic hydrogen production. X-ray photoelectron spectra (XPS) of CoP NWs (Fig. 2a and b) have been recorded to determine the covalency for Co—P bonds, which plays an important role in the transport of charge [24]. Fig. 2a shows the high resolution XPS spectrum of P2p, and the two peaks at 130.7 and 129.8 eV reflecting the binding energy of P 2p$_{1/2}$ and P 2p$_{3/2}$, respectively, along with one peak at 134.4 eV. And Fig. 2b shows two peaks at 779.2 and 782.1 eV in the Co(2p$_{3/2}$) region. The peaks at 782.1 and 134.4 eV are assigned to oxidized Co and P species, which are ascribed to the superficial oxidation of CoP [19]. Obviously, the binding energy of Co 2p (779.2 eV) is higher than metallic Co (778.4 eV), while the binding energy of P 2p (129.8 eV) is lower than elemental P (130.2 eV). That is, Co carries a partial positive charge while P carries a partial negative charge, thus electron transfer from Co to P occurs in CoP. This is reason why CoP can act as co-catalyst in photocatalytic hydrogen production. The BET specific surface area of CoP NWs is determined to be 7.1 m^2 g^{-1} by the nitrogen adsorption/desorption isotherm plot (Fig. 2c), which is larger than CoP NPs (4.1 m^2 g^{-1}). This can increase exposure and the utilization of more active sites, thus enhance the catalytic activity. Furthermore, a highly active co-catalyst must efficiently extract the photo-induced electrons from photocatalysts and transfer them to its surface, thus the excellent conductivity is needed [25]. Hence, we first investigate electrochemical performance of CoP NWs and CoP NPs. EIS is an excellent method to evaluate the electron transport property, which can be presented in the form of Nyquist plot. As can be seen from Fig. 2d, the Nyquist plots for CoP NWs and CoP NPs exhibit well-defined semicircles over the high-medium frequency region. And the smaller radius of CoP NWs can confirm a more efficient charge transfer process, which is ascribed to a smaller charge transfer resistance [26]. Afterwards, the density functional theory (DFT) calculations (Fig. 2e) are used to further understand the physical properties of CoP NWs and CoP NPs. The XRD and HRTEM data indicate that (011) crystal plane is the main growth orientation of CoP NWs. Thus, we built a supercell model exposed (011) crystal plane and a bulk model to present CoP NWs and CoP NPs, respectively (Fig. 2f) [27]. As shown in Fig. 2e, the continuous electronic states crossing Fermi level for CoP NWs and CoP NPs indicate that both of them have good conductivities. Nevertheless, the DOS near the Fermi
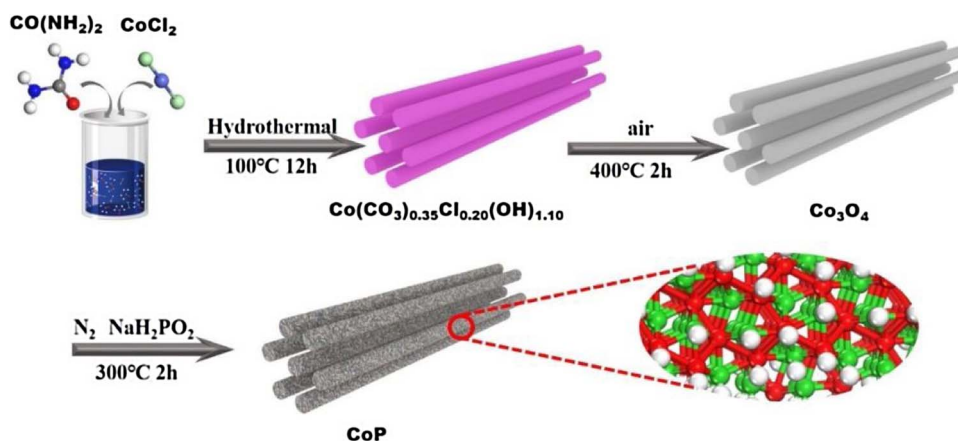
Scheme 1. Synthesis procedures of CoP NWs.

level presents the higher intensity of the electrons in CoP NWs than CoP NPs, indicating the better electrical conductivity of CoP NWs [28]. Thus, CoP NWs has a stronger capacity to accept photoinduced electrons from semiconductor photocalysts.

On the basis of the above experimental and theoretical explorations, it can be concluded that CoP NWs is a better candidate for co-catalyst in photocalytic hydrogen production than CoP NPs, which can be attributed to its larger BET SSA, excellent metallic conductivity and the rigid 1D nanostructure. Next, we will combine CoP NWs and CoP NPs with $Zn_{0.5}Cd_{0.5}S$ to evaluate their photocatalytic hydrogen production activity as co-catalysts.

3.2. Preparation and structure characterization of $Zn_{0.5}Cd_{0.5}S$/CoP NWs

Fig. 3a shows the XRD patterns of ZCS, ZCS/10% CoP NWs, ZCS/ 10% CoP NPs and the standard diffraction patterns of the cubic phase ZnS (JCPDS card no. 05-0566), hexagonal phase CdS (JCPDS card no. 41-1049). Comparing with the diffraction patterns of the cubic phase

and the hexagonal phase, the diffraction pattern of ZCS shows multi-phase characteristics. And obviously, the diffraction peaks of ZCS are shifted toward lower-angle and higher-angle side, respectively, indicating the sample is not a compound of ZnS and CdS, but a $Zn_{0.5}Cd_{0.5}S$ solid solution [22]. After mechanical mixing ZCS with CoP NWs and CoP NPs, the diffraction peaks of ZCS are not shifted and no new peaks appeared, indicating that the crystal structure of ZCS can't be affected by loading CoP (Figs. 3a and S4). As revealed by the images of SEM and TEM (Fig. 3b and c), ZCS was nanoparticles aggregation with single particle size about 20–80 nm. And the elemental mapping of ZCS clearly indicates the uniform distribution of S, Zn and Cd elements in the sample, suggesting the formation of solid solution between ZnS and CdS. And the HRTEM image (Fig. 3d) displays the clear lattice spacing of 3.25 Å, which belongs to the (111) diffraction plane of ZCS [12]. The SEM image of ZCS/10% CoP NWs (Fig. 3e) shows that CoP NWs is surrounded by ZCS nanoparticles, and there is no remarkable morphology change. Next, the TEM image (Fig. 3f) shows that some ZCS nanoparticles intimate contact with the CoP NWs, which implies
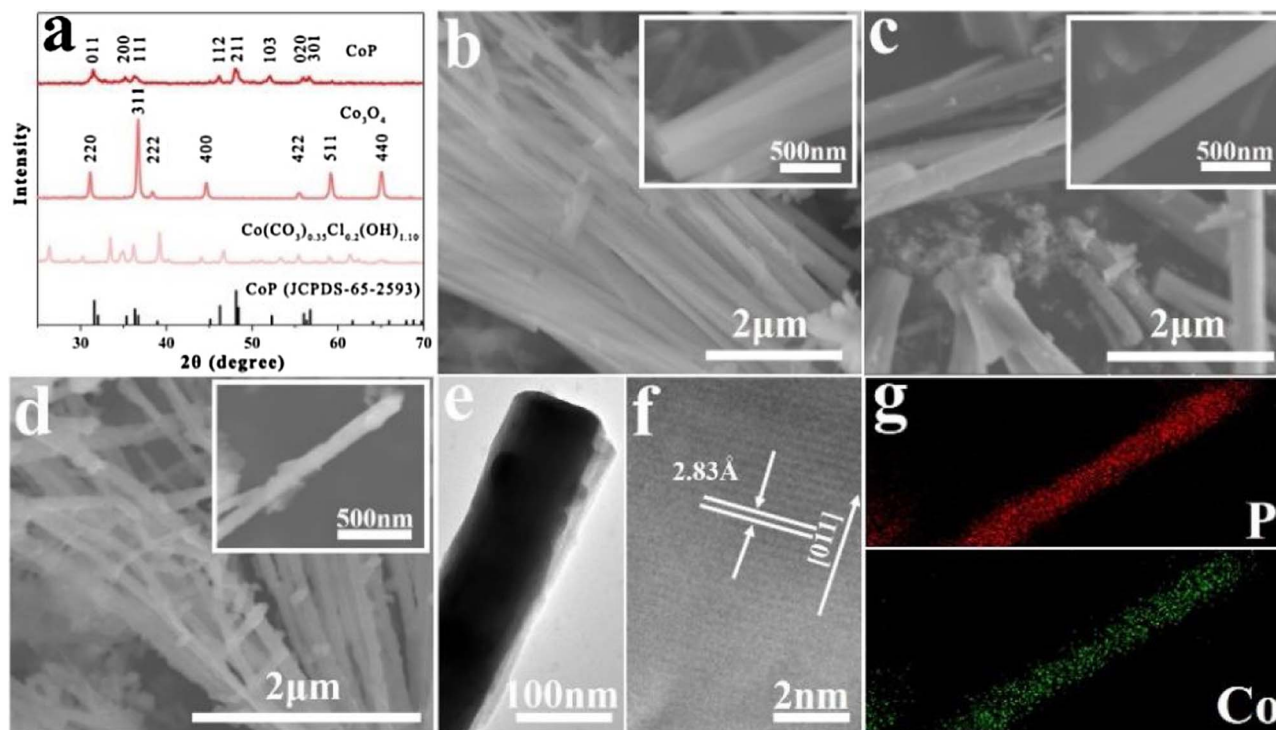

Fig. 1. (a) XRD patterns of $Co(CO_3)_{0.35}Cl_{0.20}(OH)_{1.10}$, Co_3O_4 and CoP. SEM images of (b) $Co(CO_3)_{0.35}Cl_{0.20}(OH)_{1.10}$ NWs, (c) Co_3O_4 NWs and (d) CoP NWs. TEM (e), HRTEM (f) and elemental mapping (g) images of a single CoP NWs.
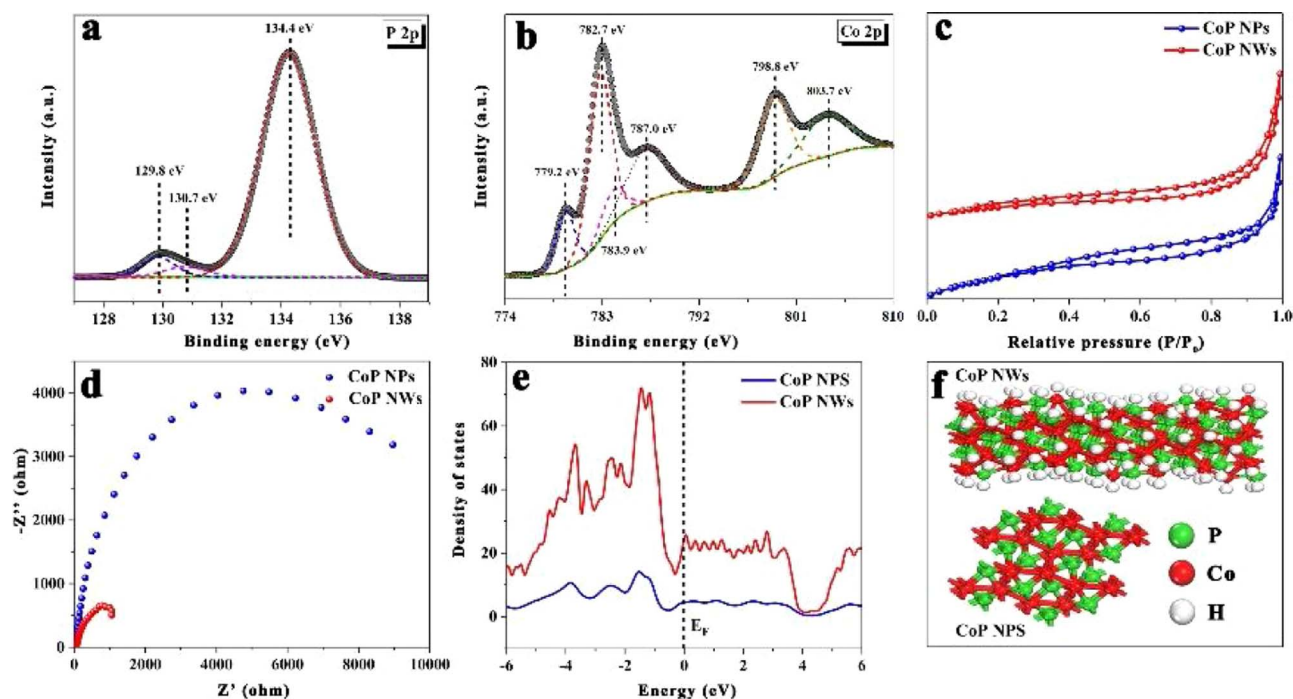
Fig. 2. XPS spectra in the (a) Co(2p$_{3/2}$) and (b) P(2p) regions for CoP NWs. (c) Nitrogen adsorption-desorption isotherms, (d) Nyquist plots, (e) calculated DOS and (f) the supercell models of CoP NWs and CoP NPs.

that chemical bonds are generated during the mixing process [21].

3.3. X-ray photoelectron spectroscopy (XPS) of ZCS and ZCS/10% CoP NWs

The chemical composition and valence states of the elements in ZCS and ZCS/10% CoP NWs are analyzed by X-ray photoelectron spectroscopy (XPS), and the binding energy is calibrated by taking the C 1s peak at 284.6 eV as reference. The presence of Zn, Cd, S, Co and P is confirmed by the spectra of the overall survey scan of ZCS and ZCS/10% CoP NWs (Fig. S5). The high resolution XPS spectra of Zn 2p and Cd 3d of the two samples are compared in Fig. 3a and b. As can be seen form Fig. 3a, the binding energies at 1023.9 and 1046.9 eV are consistent with that of Zn 2p$_{3/2}$ and 2p$_{1/2}$, respectively [29]. And the peaks located at 404.8 and 411.6 eV (Fig. 4b) can be assigned to the Cd 3d$_{5/2}$ and Cd 3d$_{3/2}$, respectively. Obviously, the above four peaks are all
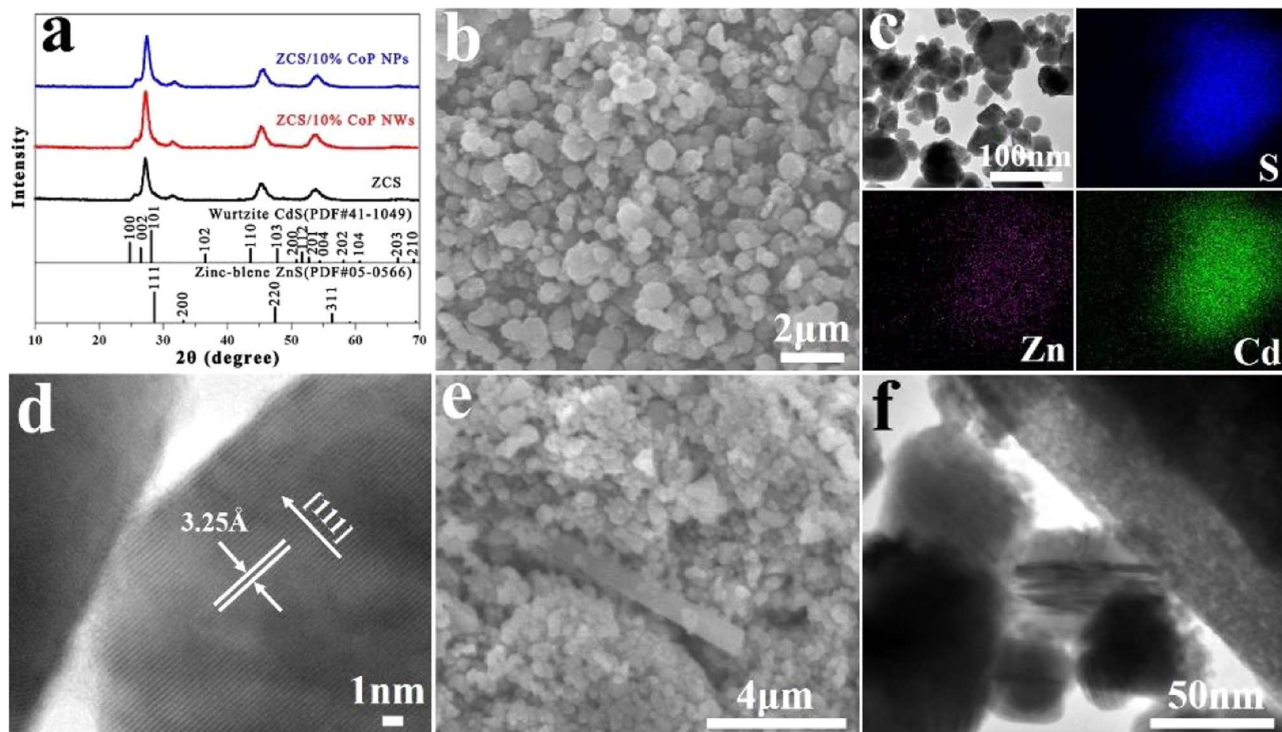

Fig. 3. (a) XRD patterns of ZCS (black), ZCS/10% CoP NWs (red) and ZCS/10% CoP NPs (blue). SEM (b), TEM and elemental mapping (c) and HRTEM (d) images of ZCS. SEM (e) and TEM (f) images of ZCS/10% CoP NWs. (For interpretation of the references to colour in this figure legend, the reader is referred to the web version of this article).

Fig. 4. The high resolution XPS spectrum of Zn 2p (a) and Cd 3d (b) of ZCS (black) and ZCS/10% CoP NWs (red), S 2p of ZCS (c) and ZCS/10% CoP NWs (d), Co 2p (e) and P 2p (f) of ZCS/10% CoP NWs. (For interpretation of the references to colour in this figure legend, the reader is referred to the web version of this article).
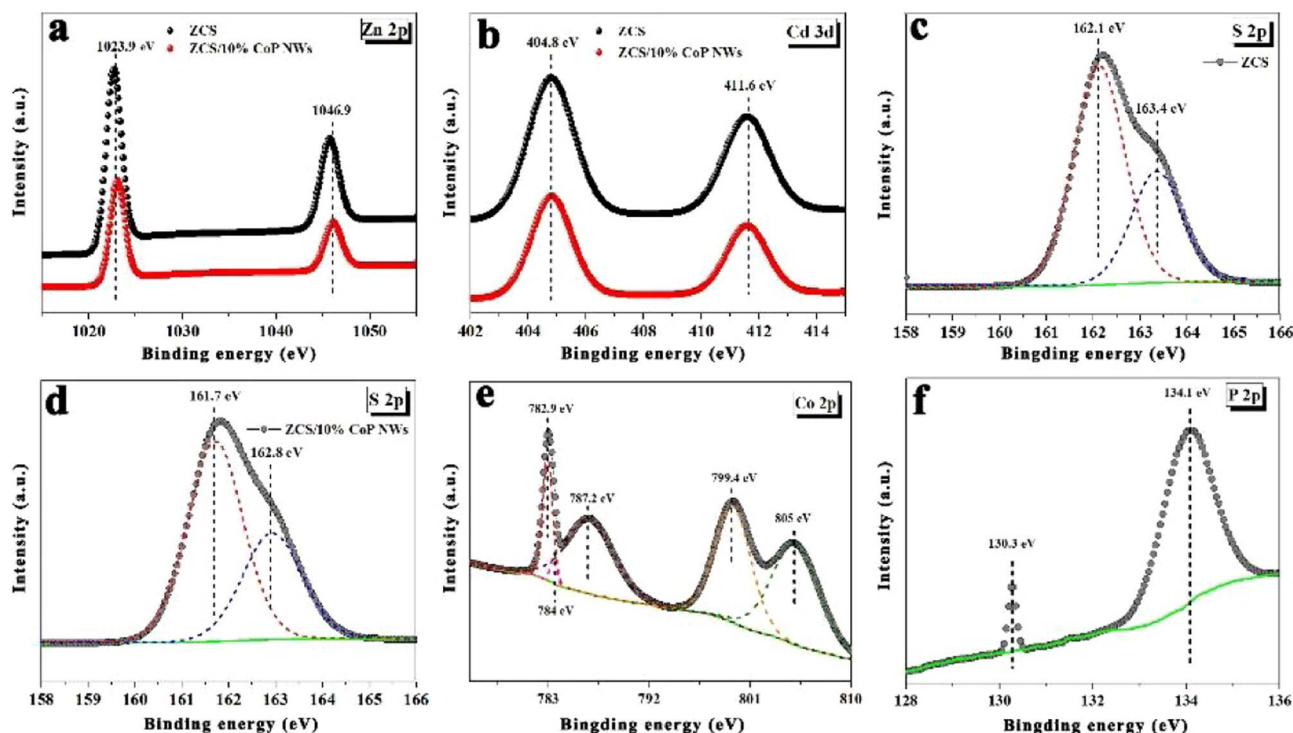
sharp and symmetrical, indicating that the valences of Zn and Cd are both +2 [12]. For S 2p (Fig. 4c and d), the band can be deconvoluted into two peaks, which can be attributed to the S $2p_{3/2}$ and S $2p_{1/2}$, respectively [30]. However, the S 2p peaks at 162.1 and 163.4 eV in ZCS shifted to lower binding energies of 161.7 and 162.8 eV in ZCS/10% CoP NWs, respectively. It can be deduced that part of S oxidized the reduced Co to form the Co−S bond [21]. And the Co−S bond between ZCS and CoP NWs would improve the charge transfer form Co to P while it would decrease the reduced Co and increase the electron density in the active sites of P for improved acceptance of protons. Meanwhile, the disappearance of the peak at 779.2 eV of reduced Co in the Co 2p XPS spectrum (Fig. 4e) after ZCS compounding indicates oxidation reaction at the interface between ZCS and CoP NWs. Generally, pure CoP is easily oxidized by air and produces the peaks at 779.2 and 134.4 eV in the Co 2p and P 2p XPS spectra, respectively [31]. However, after combining CoP with ZCS, the oxidation peak at 134.4 eV shifted to a lower binding energy of 134.1 eV, indicating a lot of charges transfer from Co to P [19]. Thus, there is a closed contact interface between ZCS and CoP, which is in accordance with the HRTEM analysis. This stronger interface interaction is beneficial to electrons transfer from ZCS photocatalyst to CoP NWs co-catalyst, which can efficiently enhance photocatalytic hydrogen production activity.

Based on the above analysis, we can conclude that the ZCS/10% CoP NWs catalyst has been successfully prepared including Zn0.5Cd0.5S solid solution photocatalyst and CoP nanowire co-catalyst. It is worth mentioning that we have actually prepared a series of catalysts containing different quantities of CoP NWs, and their photocatalytic activities will be discussed later. The photocatalytic hydrogen production results indicated that the ZCS/10% CoP NWs showed the best photocatalytic activity, so we show here only the characterization of this composite.

3.4. Photocatalytic hydrogen production of ZCS, ZCS/10% CoP NWs and ZCS/10% CoP NPs

The photoctalytic hydrogen production activity of the prepared ZCS, ZCS/x% CoP NWs and ZCS/x% CoP NPs was tested using ascorbic acid as a sacrificial agent in a typical photocatalytic reaction system. The activity of the hybrid photocatalysts showed strong dependence on the amount of CoP NWs and CoP NPs, thus we investigated the influence of the loading amount of CoP on hydrogen production. Fig. 5a displays a comparison of photocatalytic hydrogen production using ZCS/x% CoP NWs and ZCS/x% CoP NPs samples, and the loading amount of CoP is from 2% to 12%. Initially, the introduction of CoP NWs and CoP NPs concentration from 2 wt% to 10 wt% onto ZCS can gradually enhance the photocatalytic hydrogen production activity by facilitating charge collection and hydrogen production reactions. When the loading amount of CoP NWs and CoP NPs on ZCS reached 10 wt%, both of the systems achieve the highest activity. However, further loading of CoP NWs and CoP NPs drastically decrease the photocatalytic activity. This is due to the following factors: (i) excess amount of CoP NWs and CoP NPs can cover the surface active sites of ZCS and hinder its contact with sacrificial reagents or water molecules; (ii) excessive loading of CoP NWs and CoP NPs can shield the incident light and prevent the light absorption and generation of photogenerated charge; (iii) CoP NWs and CoP NPs at high loading amount can act as charge recombination centers. Thus, the optimized loading amount of CoP NWs and CoP NPs for the best hydrogen production is 10 wt%. We also can find that ZCS/x% CoP NWs shows higher photocatalytic hydrogen production rate ($12{,}175.8 \, \mu mol \, h^{-1} \, g^{-1}$) than ZCS/x% CoP NPs ($7167.9 \, \mu mol \, h^{-1} \, g^{-1}$) in each loading amount. As can be seen from Fig. 5b, ZCS/10% CoP NWs gives a hydrogen production amount of $37{,}520.2 \, \mu mol \, g^{-1}$ in 3 h, which is 22 times higher than that of the pristine ZCS ($1751.5 \, \mu mol \, g^{-1}$) and 2 times higher than that of the ZCS/10% CoP NPs ($21554.5 \, \mu mol \, g^{-1}$). These results reveal that CoP NWs is a better co-catalyst than CoP NPs, which can more efficiently enhance the photocatalytic hydrogen production of ZCS.

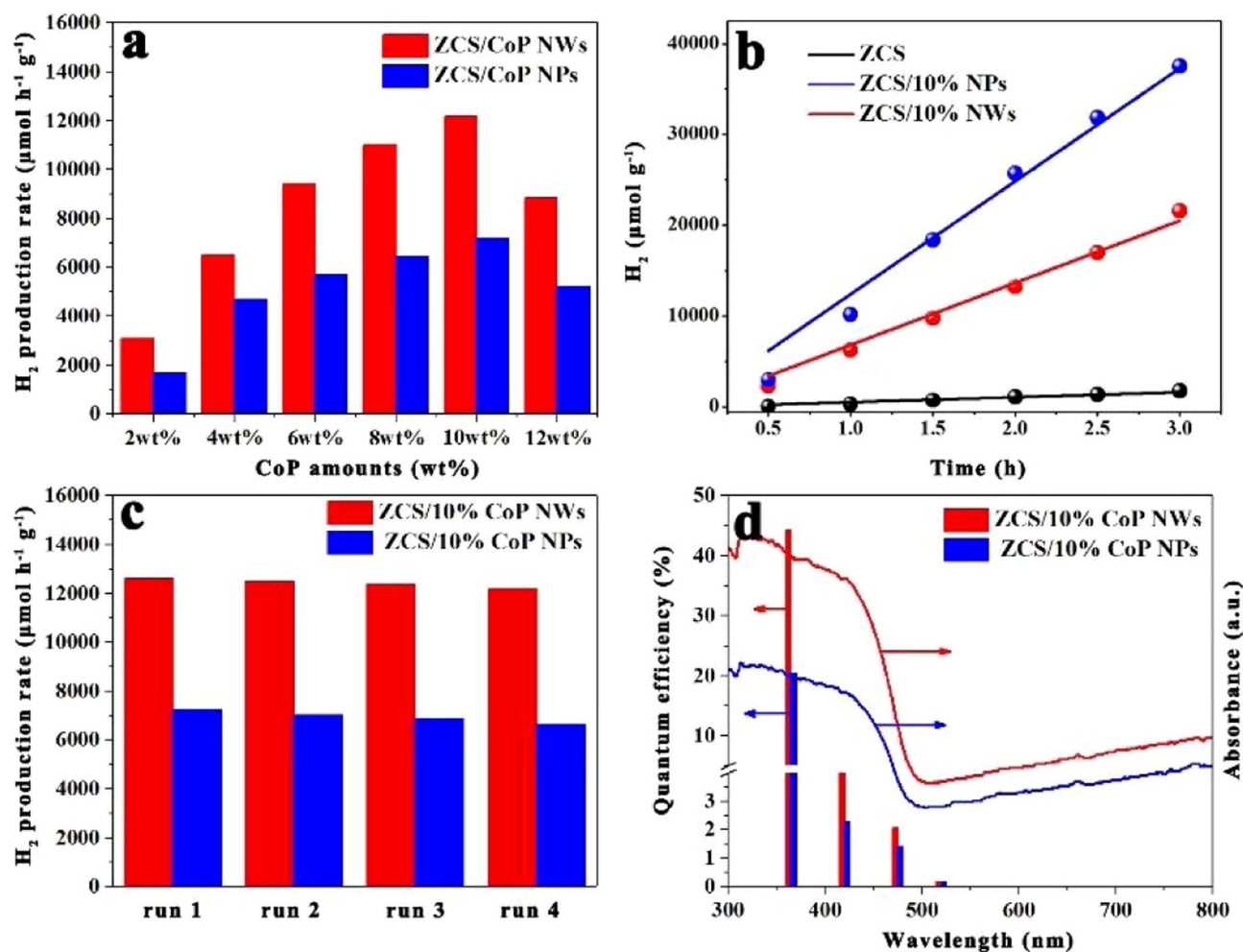In order to evaluate the stability of ZCS/10% CoP NWs, we

Fig. 5. (a) The rate of hydrogen production on ZCS loaded with different quantities of CoP NWs and CoP NPs. (b) Photocatalytic hydrogen production profile (b), the stability study (c) and quantum efficiency (d) of ZCS, ZCS/10% CoP NWs and ZCS/10% CoP NPs.

measured the hydrogen production as a function of time for several cycles as shown in Fig. 5c. During four repeated runs over a total reaction time of 12 h, the photocatalytic hydrogen production activity slightly decreases, which can be attributed to the decrease of sacrificial agent in the reaction system, indicating that the ZCS/10% CoP NWs hybrid possesses good stability for photocatalytic hydrogen production. Next, the apparent quantum efficiency (AQE) on ZCS/10% CoP NWs and ZCS/10% CoP NPs at different light wavelengths by using various band-pass filters was measured. It is well known that AQE is an alternative indicator to appropriately assess the photocatalytic efficiency of catalysts, in other words, the larger the AQE, the more efficient separation of photoinduced charge pair is, as well the photoactivity [32]. The trend in apparent quantum efficiency closely followed that of the absorbance measured by ultraviolet-visible spectroscopy (Fig. 5d), revealing bandgap-transtion-dependent hydrogen evolution behavior. Notably, ZCS/10% CoP NWs shows a high apparent quantum efficiency of about 45% at 365 nm, which is 2 times higher than ZCS/10% CoP NPs (10%). However, the AQE at 420, 475 and 520 nm are only 4.37%, 2.06% and 0.17%, respectively, resulting from the lower light absorption. At the same time, we compare the ZCS/10% CoP NWs sample with previously reported composites of $Zn_xCd_{1-x}S$ with earth abundant co-catalyst, and our photocatalyst display a comparable or higher photocatalytic activity (Table S1).

All these results as mentioned above indicated that CoP NWs is a more efficient co-catalyst than CoP NPs for hydrogen production. To explore the inherent mechanism, we take a series of measurements and discuss in the section below.

3.5. The inherent mechanism for enhanced activity of ZCS/10% CoP NWs over ZCS/10% CoP NPs

To find out the inherent mechanism for the enhancement of the photocatalytic hydrogen production activity of ZCS/10% CoP NWs over ZCS/10% CoP NPs, a series of tests were carried out. As shown in Fig. 6a, we first measured the transient photocurrent responses of the samples, which was recorded on a home-built photoelectrochemical measurement system. Generally, the photocatalyst can be excited to generate electron-hole pairs under irradiation, then the electrons and holes are oxidized and reduced on Pt foil and working electrode, respectively. The transient photocurrent response curves of the samples (also see Fig. S6) were monitored by twenty on-off cycles of intermittent irradiation, and there are fast and uniform photocurrent responses with the irradiation of light turned on and off, indicating that all the samples can act as high-quality photosensitive catalysts [33]. However, the transient photocurrent response of ZCS/10% CoP NWs is remarkably larger (7 times and 14 times) than that of ZCS/10% CoP NPs and ZCS, respectively. This result indicates that the electron and hole separation in ZCS/10% CoP NWs is much more efficient than that in ZCS/10% CoP NPs, which demonstrates that CoP NWs is more responsible for the improvement of the photocatalytic activity than CoP NPs. And this result of transient photocurrent responses matches well with the hydrogen production results (Fig. 5b). Meanwhile, the ZCS/10% CoP NWs sample shows the highest photocurrent density and the lowest photocurrent onset potential, resulting in the highest total photoconversion efficiency (Fig. S7). What's more, an appreciable IPCE
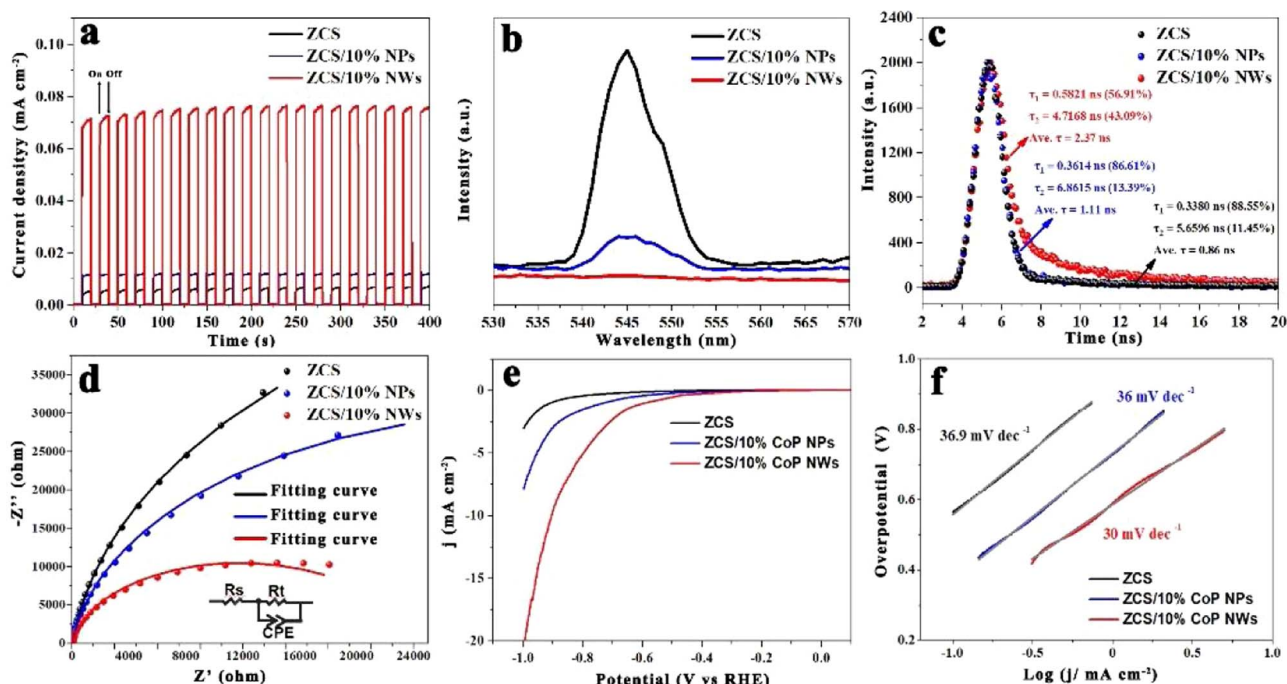
Fig. 6. Transient photocurrent responses (a), steady-state PL spectra (b), time-resolved PL decay spectra (c) and EIS Nyquist plots of ZCS, ZCS/10% CoP NWs and ZCS/10% CoP NPs.

appears when λ is less than 420 nm, indicating that the enhanced photocatalytic activities are more strongly related to the improved photoinduced electron-hole pairs separation efficiency than the broad light absorption (Fig. S8) [34]. To further investigate the charge separation and transfer behaviors in the samples, the technique of steady-state PL spectroscopy also was used. Fig. 6b shows the steady-state PL spectra of ZCS, ZCS/10% CoP NWs and ZCS/10% CoP NPs at 360 nm excitation light. Compared with ZCS and ZCS/10% CoP NPs, ZCS/10% CoP NWs shows the lowest PL peak intensity, suggesting a suppressed photoinduced charge recombination. This phenomenon further confirms that there exists faster transfer of electrons from ZCS to CoP NWs than CoP NPs, due to the better conductivity of CoP NWs.

It is well known that the charge carrier lifetime plays a key role in determining the probability of their involvement in the photocatalytic reactions before their recombination [35]. In other words, a longer charge carrier lifetime usually represents a higher possibility of their participation in the photocatalytic reactions, thus implying a better photocatalytic activity [36]. Thus, to obtain a quantitative understanding of the photoinduced charge carrier lifetime in ZCS, ZCS/10% CoP NWs and ZCS/10% CoP NPs, the time-resolved PL spectra are measured and showed in Fig. 6c. Firstly, the PL lifetimes of the samples are calculated by fitting the time-resolved PL decay curves with the following exponential fitting equation [37]:

$$\text{Fit} = A + B_1 \, exp\left\{-\frac{t}{\tau_1}\right\} + B_2 \, exp\left\{-\frac{t}{\tau_2}\right\}$$

where A, B_1 and B_2 are constants and can be obtained from the fitted decay curve. We can get two decay components containing a fast (τ_1) and a slow (τ_2) from this equation [38]. Then, based on the fitted data, the intensity-average lifetime (τ) is calculated and presented to make an overall comparison of the PL lifetimes of all samples by the following equation [39]:

$$\tau = \frac{B_1\tau_1{}^2 + B_2\tau_2{}^2}{B_1\tau_1 + B_2\tau_2}$$

Finally, we have summarized and listed the fitting PL decay data in Fig. 6c. Compared with ZCS, ZCS/10% CoP NWs and ZCS/10% CoP NPs show increased intensity-average (τ) PL lifetimes, indicating that

loading CoP co-catalysts can effectively suppress the charge recombination and elongate the lifetime of charge carriers. And obviously, ZCS/10% CoP NWs shows the longest lifetime (2.37 ns), while ZCS/10% CoP NPs shows a shorter lifetime (1.11 ns). In an obvious contrast, ZCS displays the shortest lifetime (0.86 ns). Thus, we can conclude that the lifetime of charge carriers in ZCS can be effectively lengthened by loading CoP NWs according to the above fitting data.

All of the above methods highlight the high separation and transfer efficiency of photoinduced electron-hole pairs in ZCS/10% CoP NWs upon light irradiation. However, we also need to know the charge transport process occurring in ZCS/10% CoP NWs under dark conditions, which directly revealed its ability to transfer charge carriers to the targeted reactive sites [40]. Therefore, to obtain a further understanding of the charge transport behavior in the absence of light excitation, EIS measurements were carried out under dark conditions. As can be seen from Fig. 6d, the EIS Nyquist plots of ZCS, ZCS/10% CoP NWs and ZCS/10% CoP NPs are well simulated to the equivalent electrical circuit (Fig. 6d inset), in which R_s and R_t are the electrolyte solution resistance and the interfacial charge-transfer resistance/electrolyte, respectively [40]. Based on the above model, ZCS/10% CoP NWs shows the smallest semicircle diameter and the lowest R_t value, suggesting its lowest interfacial charge-transfer resistance from electrode to electrolyte molecules. Furthermore, The electrochemical H_2 generation activities of ZCS, ZCS/10% CoP NWs and ZCS/10% CoP NPs were investigated by the LSV method. Fig. 6e gives the overpotential of different electrodes and shows that compared with ZCS and ZCS/10% CoP NPs, ZCS/10% CoP NWs has the lowest overpotential. Since the photocatalytic H_2 production is highly dependent on the overpotential of the HER reaction, the results clearly show that ZCS/10% CoP NWs is a better photocatalyst. The lowest overpotential of ZCS/10% CoP NWs (Fig. 6f) could attributed the fast transfer of electrons, which are consistent with the photocatalytic performance and photocurrent experiment.

Furthermore, we also measured the N_2 adsorption/desorption isotherms to investigate the textural effect of ZCS, ZCS/10% CoP NWs and ZCS/10% CoP NPs on photocatalytic activity. As can be seen from Fig. S11, the BET surface areas calculated for ZCS, ZCS/10% CoP NWs and ZCS/10% CoP NPs are $15.8\,m^2\,g^{-1}$, $16.7\,m^2\,g^{-1}$ and $16.9\,m^2\,g^{-1}$,
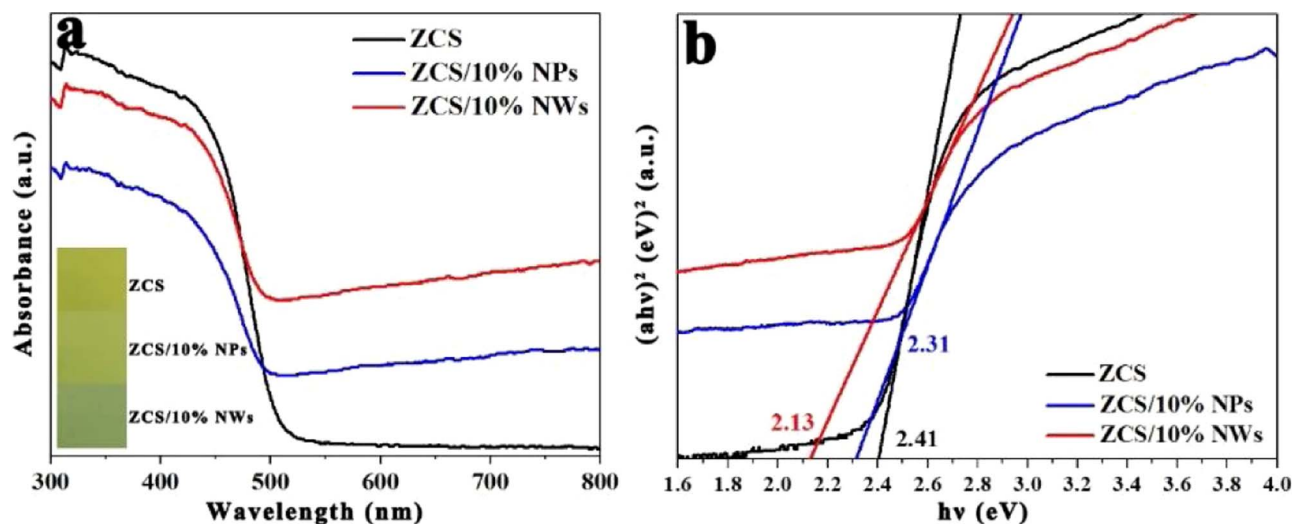
Fig. 7. UV–vis diffuse reflection spectra (a) and band-gap calculation (b) of ZCS, ZCS/10% CoP NWs and ZCS/10% CoP NPs.

respectively, whereas the average pore size distributions are all around 40 nm. The similar data suggests that the improved catalytic activity of ZCS/10% CoP NWs is not caused by the changes in the specific surface area. Thus, combined with the above analysis, CoP NWs possesses the strongest capability to separate photoinduced electron-hole pairs of ZCS and transfer the electrons to the reactant molecules adsorbed on the surface active sites, this is the key reason for the enhancement of photocatalytic hydrogen production. At last, we will propose a photocatalytic hydrogen production mechanism for this ZCS/10% CoP NWs system, which will be discuss later.

3.6. Photocatalytic hydrogen production mechanism and discussion

To gain an insight into the influence of intrinsic properties of CoP NWs on the photocatalytic activity of the hybrid, we further investigate the light-harvesting capability of ZCS/10% CoP NWs. As displayed in Fig. 7a, the light absorption of ZCS/10% CoP NWs is obviously increased in the visible region, due to the black color (Fig. 7a, inset). Similar phenomenon is also observed for ZCS/x% CoP NWs (Fig. S12). Then, based on the UV–vis diffuse reflection spectra, the band-gap (Eg) energies of the samples were obtained by the Kubelk-Munk method [41] (Fig. 7b). The band-gaps of ZCS, ZCS/10% CoP NWs and ZCS/10% CoP NPs are determined to be 2.41 eV, 2.13 eV and 2.31 eV, thus ZCS/10% CoP NWs shows a red shift of the absorption edge, suggesting the decrease of its band-gap. To gain further into the photocatalytic hydrogen production mechanism in ZCS/10% CoP NWs, the conduct band (CB) and valence band (VB) potentials of ZCS in ZCS/10% CoP NWs were determined to be −0.62 eV and 1.51 eV versus RHE, respectively (Fig. S13). Meanwhile, the CB and VB potentials of pure ZCS were determined to be −0.34 eV and 2.07 eV, respectively. Therefore, on light irradiation, the photoinduced electrons on the CB of ZCS in ZCS/10% CoP NWs can migrate to CoP NWs rapidly, which efficiently shuttle these photoinduced electrons to their surface active sites, due to its position and excellent conductivity. In a word, the function of CoP NWs in the hybrid should be like that of a metal, an electron collector and a site of H^+ reduction [42]. Thus, the CoP NWs can not only suppress the charge recombination on the surface of ZCS, but also promote the charge separation and transfer in the bulk of ZCS, which is consistent with the results mentioned above.

On the basis of the above experimental and theoretical results, a photocatalytic hydrogen production illustrating the efficiently enhance catalytic activity of ZCS/CoP NWs is proposed in Fig. 8a and b. It is well known that the photocatalytic reactions involve four consecutive steps: (i) light absorption; (ii) electron-hole pairs production; (iii) electron-

hole pairs separation and migration; (iv) surface adsorption and redox reaction[43]. And the ZCS/CoP NWs system in this work optimize the above steps and thus has an enhanced photocatalytic activity. Firstly, the electronic structure of ZCS has been modified to harvest more light. As shown in Fig. 8a, the narrowed band-gap of ZCS (2.13 eV) in ZCS/CoP NWs can extend the light absorption region to visible light region. Thus, ZCS/CoP NWs can harvest more light to photo-excite electrons in the VB to the CB, while leaving the photoinduced holes in the VB. Secondly, the CoP NWs can serve as an electron trap to efficiently capture the photoinduced electrons on the CB, thus promote the electrons transfer from ZCS to CoP NWs. Finally, the 1D nature of the CoP NWs can rapidly shuttle the electrons to its surface, meanwhile CoP NWs also can facilitate sufficient transport of reactants and products, thus obtaining the sustainable hydrogen production.

4. Conclusions

In summary, we have successfully prepared CoP nanowires through an organic solvent-free low-temperature phosphidation reaction as a high efficient co-catalyst to photocatalytic hydrogen production. On the basis of the theoretical and experimental results, 1D CoP nanowires have more outstanding features than bulk CoP nanoparticles, including larger BET specific surface area, excellent metallic conductivity and the rigid 1D nanostructure. Thus, we compounded $Zn_{0.5}Cd_{0.5}S$ solid solution and CoP NWs to investigate the photocatalytic activity of the hybrid. Remarkably, the super high photocatalytic activity of ZCS/CoP NWs hybrid (12,175.8 µmol h^{-1} g^{-1}) is 22 times higher than that of the pristine ZCS (553.4 µmol g^{-1}) and 2 times higher than that of the ZCS/10% CoP NPs (7167.9 µmol g^{-1}). By combining photoelectrochemical and time-resolved PL methodology, the outstanding activity can be ascribed to the synergetic effect of the highly efficient charge separation and migration from ZCS to CoP NWs and the rapid hydrogen production on 1D nanostructure. Successful application of 1D CoP NWs as an efficient co-catalyst on ZCS may open new avenues to develop cost-effective 1D nanostructures as co-catalyst for photocatalytic hydrogen production.
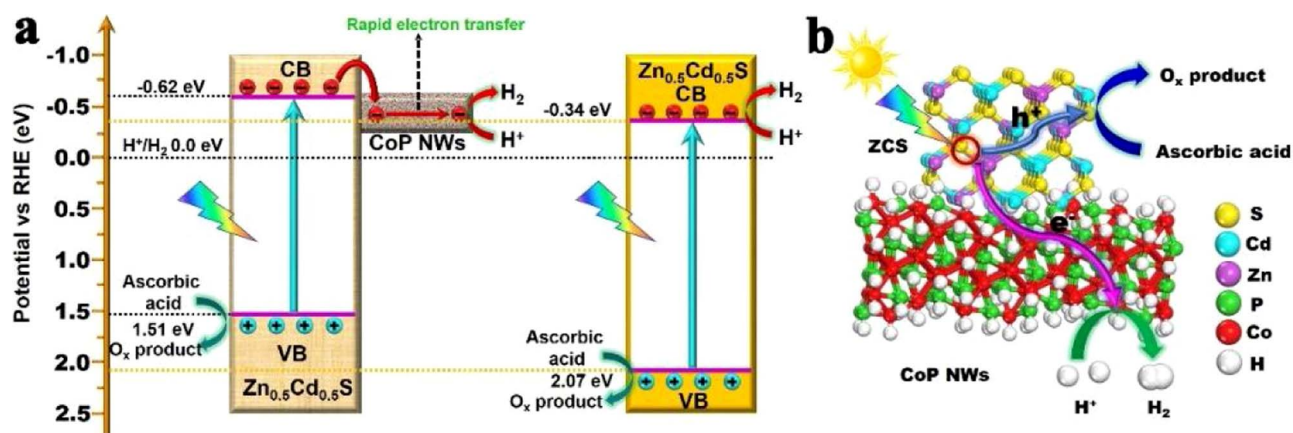
Acknowledgements

Fig. 8. (a) The charge separation and transfer in the ZCS/CoP NWs system and pure ZCS. (b) Proposed mechanism for photocatalytic hydrogen production in the ZCS/CoP NWs system.

Appendix A. Supplementary data

Supplementary material related to this article can be found, in the online version, at doi:https://doi.org/10.1016/j.apcatb.2018.02.043.

References

[1] J. Wang, W. Cui, Q. Liu, Z. Xing, A.M. Asiri, X. Sun, Adv. Mater. 28 (2016) 215–230.
[2] J. Ran, J. Zhang, J. Yu, M. Jaroniec, S.Z. Qiao, Chem. Soc. Rev. 43 (2014) 7787–7812.
[3] W. Yang, L. Zhang, J. Xie, X. Zhang, Q. Liu, T. Yao, S. Wei, Q. Zhang, Y. Xie, Angew. Chem. 128 (2016) 6828–6832.
[4] M. Hara, J. Nunoshige, T. Takata, J.N. Kondo, K. Domen, Chem. Commun. (2003) 3000–3001.
[5] K. Maeda, N. Sakamoto, T. Ikeda, H. Ohtsuka, A. Xiong, D. Lu, M. Kanehara, T. Teranishi, K. Domen, Chem. Eur. J. 16 (2010) 7750–7759.
[6] F.N. Sayed, O.D. Jayakumar, R. Sasikala, R.M. Kadam, S.R. Bharadwaj, L. Kienle, U. Schürmann, S. Kaps, R. Adelung, J.P. Mittal, A.K. Tyagi, J. Phys. Chem. C 116 (2012) 12462–12467.
[7] Q. Li, B. Guo, J. Yu, J. Ran, B. Zhang, H. Yan, J.R. Gong, J. Am. Chem. Soc. 133 (2011) 10878–10884.
[8] S.R. Lingampalli, U.K. Gautam, C.N.R. Rao, Energy Environ. Sci. 6 (2013) 3589–3594.
[9] K. Wu, H. Zhu, Z. Liu, W. Rodríguez-Córdoba, T. Lian, J. Am. Chem. Soc. 134 (2012) 10337–10340.
[10] M. Murdoch, G.I.N. Waterhouse, M.A. Nadeem, J.B. Metson, M.A. Keane, R.F. Howe, J. Llorca, H. Idriss, Nat. Chem. 3 (2011) 489–492.
[11] S. Onsuratoom, T. Puangpetch, S. Chavadej, Chem. Eng. J. 173 (2011) 667–675.
[12] J. Song, H. Zhao, R. Sun, X. Li, D. Sun, Energy Environ. Sci. 10 (2017) 225–235.
[13] Z.J. Sun, H.F. Zheng, J.S. Li, P.W. Du, Energy Environ. Sci. 8 (2015) 2668–2676.
[14] Z.J. Sun, Q.D. Yue, J.S. Li, J. Xu, H.F. Zheng, P.W. Du, J. Mater. Chem. A 3 (2015) 10243–10247.
[15] Z.J. Sun, H.L. Chen, Q. Huang, P.W. Du, Catal. Sci. Technol. 5 (2015) 4964–4967.
[16] Q.D. Yue, Y.Y. Wan, Z.J. Sun, X.J. Wu, Y.P. Yuan, P.W. Du, J. Mater. Chem. A 3 (2015) 16941–16947.
[17] S. Cao, Y. Chen, C.C. Hou, X.J. Lv, W.F. Fu, J. Mater. Chem. A 3 (2015) 6096–6101.
[18] S. Cao, Y. Chen, C.J. Wang, X.J. Lv, W.F. Fu, Chem. Commun. 51 (2015) 8708–8711.
[19] P. Jiang, Q. Liu, C.J. Ge, W. Cui, Z.H. Pu, A.M. Asiri, X.P. Sun, J. Mater. Chem. A 2 (2014) 14634–14640.
[20] J. Tian, N. Cheng, Q. Liu, W. Xing, X. Sun, Angew. Chem. Int. Ed. 54 (2015) 5493–5497.
[21] B.C. Qiu, Q.H. Zhu, M.Y. Xing, J.L. Zhang, Chem. Commun. 53 (2017) 897–900.
[22] M.C. Liu, D.W. Jing, Z.H. Zhou, L.J. Guo, Nat. Commun. 4 (2013) 2278.
[23] S.Y. Zhang, E.Y. Ye, S.H. Liu, S.H. Lim, S.Y. Tee, Z.L. Dong, Adv. Mater. 24 (2012) 4369–4375.
[24] Z. Yang, L. Liu, X. Wang, S. Yang, X. Su, J. Alloys Compd. 509 (2011) 165–171.
[25] J. Ran, G. Gao, F. Li, T. Ma, A. Du, S.Z. Qiao, Nat. Commun. 8 (2017) 13907.
[26] M.S. Faber, R. Dziedzic, M.A. Lukowski, N.S. Kaiser, Q. Ding, S. Jin, J. Am. Chem. Soc. 136 (2014) 10053–10061.
[27] Z. Jin, P. Li, D. Xiao, Green Chem. 18 (2016) 1459–1464.
[28] K. Xu, P.Z. Chen, X.L. Li, Y. Tong, H. Ding, X.J. Wu, W.S. Chu, Z.M. Peng, C.Z. Wu, Y. Xie, J. Am. Chem. Soc. 137 (2015) 4119–4125.
[29] S.N. Guo, Y.L. Min, J.C. Fan, Q.J. Xu, ACS Appl. Mater. Interfaces 8 (2016) 2928–2934.
[30] S.J. Zhao, J.J. Huang, Q.Y. Huo, X.Z. Zhou, W.X. Tu, J. Mater. Chem. A 4 (2016) 193–199.
[31] H. Zhao, P.P. Jiang, W. Cai, Chem. Asian J. 12 (2017) 361–365.
[32] C.X. Zhao, H. Luo, F. Chen, P. Zhang, L.H. Yi, K.Y. You, Energy Environ. Sci. 7 (2014) 1700–1707.
[33] Y. Tian, L.G. Wang, H.Q. Tang, W.W. Zhou, J. Mater. Chem. A 3 (2015) 11294–11301.
[34] Y.F. Xu, C. Zhang, L.X. Zhang, X.H. Zhang, H.L. Yao, J.L. Shi, Energy Environ. Sci. 9 (2016) 2410–2417.
[35] J. Ran, T.Y. Ma, G. Gao, X.-W. Du, S.Z. Qiao, Energy Environ. Sci. 8 (2015) 3708–3717.
[36] P. Niu, L.L. Zhang, G. Liu, H.M. Cheng, Adv. Funct. Mater. 22 (2012) 4763–4770.
[37] X.H. Zhang, L.J. Yu, C.S. Zhuang, T.Y. Peng, R.J. Li, X.G. Li, ACS Catal. 4 (2014) 162–170.
[38] Y.C. Chen, T.C. Liu, Y.J. Hsu, ACS Appl. Mater. Interfaces 7 (2015) 1616–1623.
[39] Z.Y. Zhang, J.D. Huang, M.Y. Zhang, L. Yuan, B. Dong, Appl. Catal. B 163 (2015) 298–305.
[40] J.R. Ran, J. Zhang, J.G. Yu, S.Z. Qiao, ChemSusChem 7 (2014) 3426–3434.
[41] H. Yaghoubi, Z. Li, Y. Chen, H.T. Ngo, V.R. Bhethanabotla, B. Joseph, S.Q. Ma, R. Schlaf, A. Takshi, ACS Catal. 5 (2015) 327–335.
[42] K. Chang, Z.W. Mei, T. Wang, Q. Kang, S.X. Ouyang, J.H. Ye, ACS Nano 8 (2014) 7078–7087.
[43] S.S. Chen, S. Shen, G.J. Liu, Y. Qi, F.X. Zhang, C. Li, Angew. Chem. Int. Ed. 54 (2015) 3047–3051.